

# Tensegrity Robot Proprioceptive State Estimation with Geometric Constraints

Wenzhe Tong, Tzu-Yuan Lin, Jonathan Mi, Yicheng Jiang, Maani Ghaffari, and Xiaonan Huang

**Abstract**—Tensegrity robots, characterized by a synergistic assembly of rigid rods and elastic cables, form robust structures that are resistant to impacts. However, this design introduces complexities in kinematics and dynamics, complicating control and state estimation. This work presents a novel proprioceptive state estimator for tensegrity robots. The estimator initially uses the geometric constraints of 3-bar prism tensegrity structures, combined with IMU and motor encoder measurements, to reconstruct the robot’s shape and orientation. It then employs a contact-aided invariant extended Kalman filter with forward kinematics to estimate the global position and orientation of the tensegrity robot. The state estimator’s accuracy is assessed against ground truth data in both simulated environments and real-world tensegrity robot applications. It achieves an average drift percentage of 4.2%, comparable to the state estimation performance of traditional rigid robots. This state estimator advances the state of the art in tensegrity robot state estimation and has the potential to run in real-time using onboard sensors, paving the way for full autonomy of tensegrity robots in unstructured environments.

## I. INTRODUCTION

Tensegrity robots are composed of rigid rods suspended by a network of cables or tendons. This tensional integrity structural design enhances the robot’s resilience, allowing it to absorb impacts and undergo deformation without losing functionality [1], [2]. By modulating the cable length, the robots can morph their shape on the fly, enabling them to maneuver through constrained environments and traverse unstructured terrains. Most existing research on tensegrity robots has predominantly focused on their design [3]–[6], control [7]–[9], and dynamics [2], [7], with relatively limited attention given to the challenge of state estimation. The inherent flexibility and deformable structure of the design, combined with their unique rolling maneuver, introduce significant challenges in accurately reconstructing the robots’ shape and estimating their pose.

Autonomous robots with motion planning and feedback control capabilities rely extensively on accurate state estimation, i.e., position, orientation, and velocity. Exteroceptive sensors, e.g., cameras, LiDARs, are commonly used to provide perceptual data for global localization and navigation [10], [11]. However, these sensors typically operate at low frequencies (10–30Hz) and are susceptible to featureless scenarios [12], [13] and motion blurs [14]. In contrast, proprioceptive sensors, e.g., IMUs and joint encoders, are more robust against external disturbances such as illumination changes and can run at high frequencies (50–1000Hz).

<sup>1</sup>The authors are with the University of Michigan-Ann Arbor, Ann Arbor, MI, 48109, USA. {wenzhet, tzuyuan, jjomi, valeska, maanigj, xiaonanh}@umich.edu

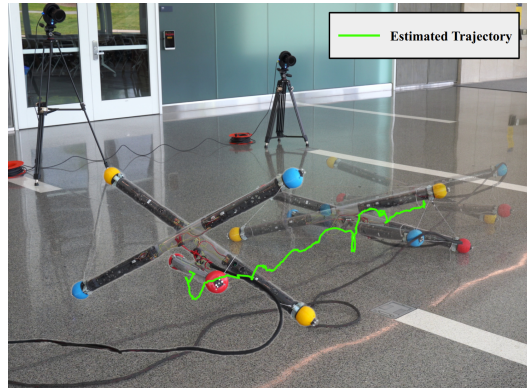


Fig. 1: Tensegrity robot state estimation experiment setup, the robot is teleoperated to roll on a flat ground.

Many existing tensegrity robots are often sensor-free [7], [8], [15]–[17], making them incapable of performing independent state estimation, or they rely on external sensors to achieve this functionality. Only a few tensegrity robots [18]–[20] can estimate their shape using onboard sensors, but they lack the capability for pose estimation. Conventional vision-based pose estimation techniques [10], [21] prove challenging due to the deformable nature of the tensegrity robots and issues related to self-occlusion. This underscores the need to develop robust, high-frequency proprioceptive state estimators that utilize onboard sensors. To the best of our knowledge, no tensegrity robot currently possesses the capability for state estimation relying solely on proprioceptive sensors, which significantly hinders the application of tensegrity robots in real-world exploration tasks.

In this paper, we developed a proprioceptive state estimator for the tensegrity robot using an invariant extended Kalman filter (InEKF). The proposed method estimates the robot shape in the body frame as kinematics information, further integrating the inertial measurements to estimate the robot’s position and orientation. The method is evaluated quantitatively in both Mujoco simulation and real-world settings, where the tensegrity robot is locomoted using pre-computed gaits. The estimated pose is compared to ground truth obtained from the simulation or a motion capture system, and achieves an average of 4.2% final drift percentage, comparable to wheeled robots at 3.8%, legged robots at 1.65% and full-size vehicles at 3.18% as reported in [13].

The contributions of this paper are:

- 1) We propose the first proprioceptive InEKF state estimator that can estimate both the shape and pose of tensegrity robot system, introducing a measurement model tailored to the kinematics of tensegrity robots.

- 2) We incorporate the geometric properties of the 3-bar tensegrity robot as constraints in the robot shape reconstruction process using constrained optimization.
- 3) We validated the effectiveness of the proposed method through both simulation and hardware experiments conducted with the 3-bar tensegrity robot rolling on flat terrain.
- 4) The code can be accessed at: <https://github.com/Jonathan-Twz/tensegrity-robot-state-estimator>

## II. RELATED WORK

Proprioceptive state estimation problems for traditional rigid robots are well-studied. For legged robots, the initial proprioceptive state estimation methods were based on leg kinematics, known as legged odometry (LO) [22], [23]. Legged odometry assumes the contact foot is static in the world frame, and the robot’s state is estimated using the motion of the legs, including position and orientation, through forward kinematics based on joint angles and foot contacts. More recent work has focused on incorporating IMU data with legged odometry (LIO) using Kalman Filter (KF) [24]. Bloesch et al. [25] proposed estimating robot pose, velocity, and IMU biases using body IMU, joint encoders, and foot contact sensors. Hartley et al. [26] designed a contact-aided Invariant Extended Kalman Filter (InEKF) for legged robot state estimation. The IMU strapdown model was used for propagation, while foot contact positions were augmented in the state during the correction step using forward kinematics. The contact-aided InEKF improved orientation estimation convergence and overall performance on the bipedal Cassie robot.

Wheeled robots and autonomous vehicles, on the other hand, utilize data from IMU and wheel encoders to provide robust state estimates, even in the presence of collisions or slippage events [27], [28]. Legged and wheeled robots benefit from deterministic kinematics, where control inputs are directly mapped to body velocity. However, tensegrity robots pose a unique challenge, as their control algorithms and kinematics depend on continuously changing shapes. This makes it crucial to estimate both the robot’s shape and pose in real-time.

For shape reconstruction, which involves estimating the endcap positions within the body frame using onboard sensors, several approaches have been explored. Elastic stretch sensors, as demonstrated in [18], [29], can estimate the distance between two cable-connected endcaps. In [5], motor encoders provide accurate cable length measurements for the nylon cables connecting the endcaps. IMUs installed on the structure can estimate the robot’s orientation [30]. Li et al. [20] proposed a new shape recognition method using elastic cable length sensors and recurrent neural network (RNN), although this approach overlooks the tensegrity robot’s geometrical properties. Booth et al. [31] developed a sensor skin with conductive capacitive strain sensors to measure the distance between adjacent endcaps and used optimization to determine the endcap positions within the local reference frame.

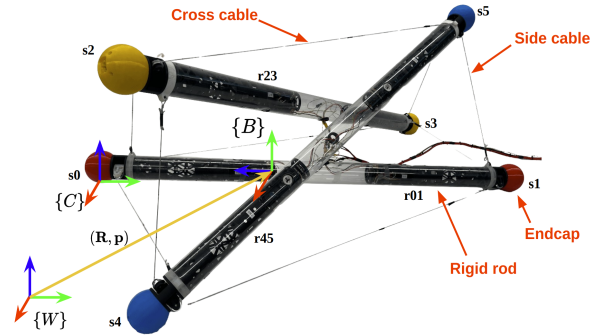


Fig. 2: Tensegrity robot structure and coordination frames. Orientation  $\mathbf{R}_t$  and position  $\mathbf{p}_t$  of the robot are represented with respect to the world frame ( $\mathbf{W}$ ). The IMU measurements  $\mathbf{a}_t, \omega_t$  are in the IMU frame, which is aligned with the Body frame ( $\mathbf{B}$ ).

For pose estimation, Moldagalieva et al. [32] proposed a vision-based method for arm-like tensegrity robots using fiducial markers assuming that the markers remain visible to overhead cameras. Previous work [33] combined proprioceptive and exteroceptive sensors, using an Unscented Kalman Filter (UKF) to estimate global rods poses by fusing data from IMU and (Ultra-Wideband) UWB positioning sensor placed at the endcaps of the rods. More recently, Lu et al. [18] track the 6-DoF pose of each rod using overhead depth and RGB images, combined with cable length measurements from onboard stretch sensors. Their method uses the correspondence between depth and RGB images to estimate rod poses during the transition step. In the correction step, joint-constrained optimization is performed with rod pose estimates and cable length measurements, to refine estimates of the global rod poses.

In summary, while some progress has been made in shape and pose state estimation for tensegrity robots, no fully proprioceptive state estimator has been developed for tensegrity robots, which is the focus of this work.

## III. PROBLEM FORMULATION

### A. Robot definition

As shown in Fig. 2, the 3-bar triangular prism tensegrity robot consists of three identical rigid rods with endcaps on each end. The endcaps on the same side denoted as  $\{s_0, s_2, s_4\}$  and  $\{s_1, s_3, s_5\}$  in Fig. 2—are connected by three length controlled side cables. The endcaps on one end of each rod are also connected to the opposite endcaps of adjacent rods by three cross cables arranged in a counterclockwise configuration, mimicking elastic springs. The shape-morphing capability is leveraged to enable rolling locomotion by shifting the robot’s center of mass.

Unlike other robots, the tensegrity robot is rotational symmetric, complicating the definition of a fixed robot base—essential for establishing the mathematical representation and kinematics of the robots. To address this, we designate the rod  $r_{01}$  in Fig. 2 as the base rod. The origin of the robot’s body frame is defined at the position of the IMU, installed near the center of this base rod, denoted as  $c_{01}$ , with an offset of  $d_{\text{offset}}$  towards  $s_0$ . The z-axis is aligned along the axial direction of the base rod. This specific frame definition

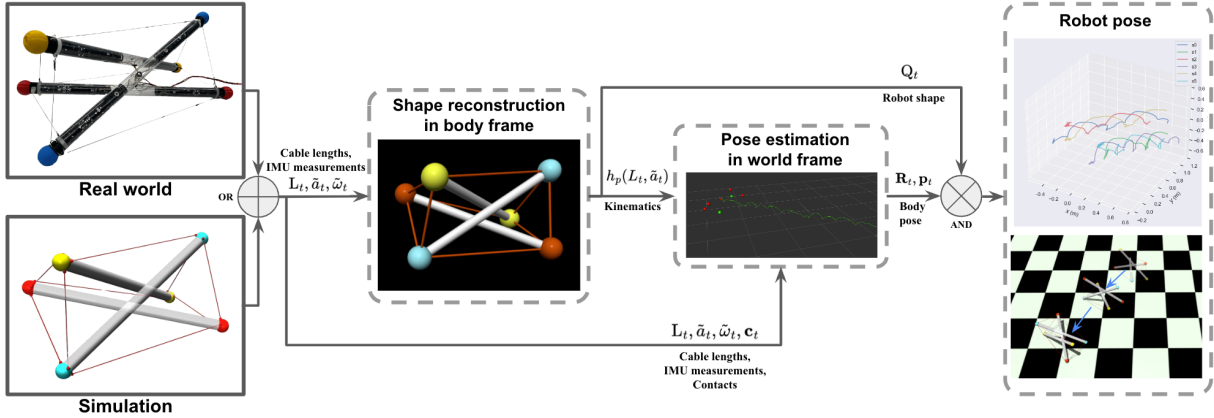


Fig. 3: Tensegrity robot state estimation framework. Firstly, the real-world or simulated IMU and cable length sensors are input into an optimization-based robot shape reconstruction algorithm, as discussed in Sec. V-A. The reconstructed shape provides the positions of the robot’s endcaps in the body frame. Next, the computed kinematics, based on the contact points between the endcaps and ground, are utilized within a contact-aided Invariant EKF to estimate the robot pose. Finally, the global endcap positions are computed by transforming the reconstructed shape into the body pose within a global frame.

is critical for developing the kinematic model and accurately describing the robot’s motion.

### B. Problem definition

This work aims to track the **pose** of the 3-bar tensegrity robot and the **robot shape** in body frame. i.e.,

- Tensegrity robot body pose in world frame at time  $t$ :  $\mathbf{x}_t \in \text{SE}(3)$ ,
- Endcap positions in body frame at time  $t$ :  $Q_t = \{\mathbf{q}_t^i | i \in \{0, 1, 2, 3, 4, 5\}\} \subset \mathbb{R}^3$ .

Given the sensor measurements and priors:

- IMU acceleration and angular velocity measurements at time  $t$ :  $\tilde{a}_t, \tilde{\omega}_t$ ,
- Cable length measurements  $L_t = \{\tilde{l}_t^{ij} | (i, j) \in \mathbb{E}\}$ , where  $i, j$  are the endcap ids. Here,  $\mathbb{E}$  represents a set of pairs corresponding to the endcap ids connected by the actuated cables. Specifically,

$$\mathbb{E} = \{(0, 4), (0, 2), (2, 4), (1, 5), (1, 3), (3, 5), (1, 4), (0, 3), (2, 5)\}. \quad (1)$$

- Endcap positions in body frame at  $t - 1$  time stamp:  $Q_{t-1} = \{\mathbf{q}_{t-1}^i | i \in \{0, 1, 2, 3, 4, 5\}\} \subset \mathbb{R}^3$ .
- $L_{\text{rod}}$  is a constant that represents the rigid bar’s length,

## IV. METHODOLOGY

The proprioceptive state estimation for the tensegrity robot inherits the legged robot state estimation frameworks in [13], [26], while the legged kinematic chain is substituted by the kinematics from the contact points to the robot base via tensegrity robot shape reconstruction in body frame. The framework overview is illustrated in Fig. 3.

Our assumptions are as follows:

- All nine cable lengths can be accurately measured for robot shape reconstruction. This can be achieved by using stretch sensors [18], [19] or motor encoders [5].
- Contact events between the robot endcap and ground can be reliably detected.
- The endcap-ground contact is modeled as point contact and remains static in the single contact period.

### A. State Representation on Lie Group

In robot state estimations, our focus is on the robot’s orientation, velocity, and position relative to a fixed world frame. We denote the rotational matrix  $\mathbf{R}_t \in \text{SO}(3)$  to represent the transformation from the body frame to the world frame and  $\mathbf{v}_t \in \mathbb{R}^3$  and  $\mathbf{p}_t \in \mathbb{R}^3$  as the body velocity and position in the world frame, respectively. In InEKF framework [26], [27], the state is defined in direct isometries group  $\mathbf{x}_t \in \text{SE}_{1+2}(3)$  [13], [34]–[36]:

$$\mathbf{x}_t := \begin{bmatrix} \mathbf{R}_t & \mathbf{v}_t & \mathbf{p}_t & \mathbf{d}_t^1 & \cdots & \mathbf{d}_t^l \\ \mathbf{0}_{l+2,3} & & & \mathbf{I}_{l+2} & & \end{bmatrix}, \quad (2)$$

where  $\mathbf{d}_t^l \in \mathbb{R}^3$  is added as augmented states for foot contact position in the world frame if valid static contact exists.

### B. IMU Propagation

The IMU measures acceleration  $a_t \in \mathbb{R}^3$  and angular velocity  $\omega_t \in \mathbb{R}^3$ . We model the IMU measurements as being corrupted by additive multivariate Gaussian noise:

$$\begin{aligned} \tilde{a}_t &= a_t + b_t^a + w_t^a, & w_t^a &\sim \mathcal{N}(\mathbf{0}_{3,1}, \Sigma_a), \\ \tilde{\omega}_t &= \omega_t + b_t^g + w_t^g, & w_t^g &\sim \mathcal{N}(\mathbf{0}_{3,1}, \Sigma_g). \end{aligned} \quad (3)$$

We assume that the endcap contact position in the world frame remains static throughout the contact period. However, in order to compensate for slippage and other uncertainties, we model the contact velocity as Gaussian white noise  $w_t^d \sim \mathcal{N}(0, \Sigma^d)$ . The unbiased continuous system dynamics can then be expressed as:

$$\frac{d}{dt} \mathbf{R}_t = \mathbf{R}_t (\tilde{\omega}_t - w_t^g)_\times, \quad \frac{d}{dt} \mathbf{v}_t = \mathbf{R}_t (\tilde{a}_t - w_t^a) + \mathbf{g}, \quad (4a)$$

$$\frac{d}{dt} \mathbf{p}_t = \mathbf{v}_t, \quad \frac{d}{dt} \mathbf{d}_t = \mathbf{R}_t h_R(L_t, \tilde{a}_t) (-w_t^d), \quad (4b)$$

where  $(\cdot)_\times$  denotes the 3x3 skew-symmetric matrix,  $\mathbf{g}$  represents the gravity vector,  $L_t$  is the cable length measurements, and  $h_R(L_t, \tilde{a}_t)$  represents the orientation of the contact frame

from the shape optimization, which we will discuss in Sec. V-A. We follow the method in [26] to account for the system's biases.

Rewriting into the matrix form, we have:

$$\begin{aligned} \frac{d}{dt} \mathbf{x}_t &= \begin{bmatrix} \mathbf{R}_t(\tilde{\omega}_t) \times & \mathbf{R}_t \tilde{a}_t + \mathbf{g} & \mathbf{v}_t & \mathbf{0}_{3,1} \\ \mathbf{0}_{1,3} & 0 & 0 & 0 \\ \mathbf{0}_{1,3} & 0 & 0 & 0 \\ \mathbf{0}_{1,3} & 0 & 0 & 0 \end{bmatrix} \\ &- \begin{bmatrix} \mathbf{R}_t & \mathbf{v}_t & \mathbf{p}_t & \mathbf{d}_t \\ \mathbf{0}_{1,3} & 1 & 0 & 0 \\ \mathbf{0}_{1,3} & 0 & 1 & 0 \\ \mathbf{0}_{1,3} & 0 & 0 & 1 \end{bmatrix} \begin{bmatrix} (w_t^g) \times & w_t^a & 0 & h_R(L_t, \tilde{a}_t) w_t^d \\ \mathbf{0}_{1,3} & 0 & 0 & 0 \\ \mathbf{0}_{1,3} & 0 & 0 & 0 \\ \mathbf{0}_{1,3} & 0 & 0 & 0 \end{bmatrix} \\ &:= f_{u_t}(\mathbf{x}_t) - \mathbf{x}_t \mathbf{w}_t^\wedge, \end{aligned} \quad (5)$$

where,  $\mathbf{w}_t := \text{vec}(w_t^g, w_t^a, \mathbf{0}_{3,1}, h_R(L_t, \tilde{a}_t) w_t^d)$  and  $u_t := [(\tilde{\omega}_t)^\top, (\tilde{a}_t)^\top]^\top \in \mathbb{R}^6$ . We can verify that the dynamic function  $f_{u_t}(\cdot)$  satisfies the group affine condition and the right invariant error is defined as:  $\eta_t^r = \bar{X}_t X_t^{-1} = (\bar{X}_t L)(X_t L)^{-1}$ , where,  $\bar{X}_t$  and  $X_t$  represent two trajectories in the group  $\mathcal{G}$ , and  $L \in \mathcal{G}$  is an arbitrary element of the group.

Then, the right-invariant error dynamics [26] is:

$$\begin{aligned} \frac{d}{dt} \eta_t^r &= f_{u_t}(\eta_t^r) - \eta_t^r f_{u_t}(I) + (X_t \omega_t^\wedge X_t^{-1}) \eta_t^r \\ &:= g_{u_t}(\eta_t^r) + \omega_t^\wedge \eta_t^r \end{aligned} \quad (6)$$

Then, from [35], we can obtain the right-invariant state-independent linearized error dynamics by deriving  $A_t^r$  from  $g_{u_t}(\eta_t) = g_{u_t}(\exp(\xi_t)) := (A_t \xi_t)^\wedge + \mathcal{O}(\|\xi_t\|^2)$ :

$$\frac{d}{dt} \xi_t^r = A_t^r \xi_t^r - \text{Ad}_{\bar{X}_t} w_t, \quad A_t^r = \begin{bmatrix} 0 & 0 & 0 & 0 \\ (\mathbf{g}) \times & 0 & 0 & 0 \\ 0 & \mathbf{I} & 0 & 0 \\ 0 & 0 & 0 & 0 \end{bmatrix} \quad (7)$$

In summary, with  $A_t^r$  in, the state estimate  $\bar{\mathbf{x}}_t$  is propagate through the system dynamics  $f_{u_t}(\cdot)$ . And the covariance matrix  $P_t^r$  is computed using the Riccati equation:

$$\begin{aligned} \frac{d}{dt} \bar{\mathbf{x}}_t &= f_{u_t}(\bar{\mathbf{x}}_t) \\ \frac{d}{dt} P_t^r &= A_t^r P_t^r + P_t^r A_t^{r\top} + \text{Ad}_{\bar{\mathbf{x}}_t} \text{Cov}(w_t) \text{Ad}_{\bar{\mathbf{x}}_t}^\top \end{aligned} \quad (8)$$

### C. Forward Kinematics Correction

Endcap contacts provide additional constraints for estimating the tensegrity robot's state by assuming contact velocity is zero in the world frame.

The contact state  $C$  is defined as a binary vector  $\mathbf{c}_t = [c_0, c_1, c_2, c_3, c_4, c_5]$ , where  $c_i \in \{0, 1\}$  for each endcap  $s_i$ . The contact state can be estimated using a robot shape and IMU reading or an external contact sensor.

1) *Contact State Augmentation*: Once the contact event  $C$  is detected, we append the contact state into the state variable using the optimized robot shape information in Sec. V-A, which is:  $\mathbf{d}_t^i = \mathbf{p}_t + \mathbf{R}_t h_p(L_t, \tilde{a}_t)$ , where  $h_p(\cdot)$  is the optimization function that takes the cable length measurements and IMU accelerometer readings to calculate

the ground-contact endcap position in the body frame. The corresponding covariance can be augmented using:

$$\begin{aligned} P_{t_k}^{\text{new}} &= F_t P_t F_t^\top + G_t \text{Cov}(w_t^a) G_t^\top, \\ F_{t_k} &= \begin{bmatrix} \mathbf{I} & 0 & 0 \\ 0 & \mathbf{I} & 0 \\ 0 & 0 & \mathbf{I} \\ 0 & 0 & \mathbf{I} \end{bmatrix}, \quad G_{t_k} = \begin{bmatrix} 0 \\ 0 \\ 0 \\ \bar{R}_{t_k} J_p(L_t, \tilde{a}_t) \end{bmatrix}, \end{aligned} \quad (9)$$

where  $J_p(\cdot)$  is the Jacobian of  $h_p(\cdot)$ . For the tensegrity robot, the  $h_p(\cdot)$  is formulated as an optimization problem, and we cannot derive the Jacobian analytically. Instead, we treat it as a tunable parameter and empirically determine the covariance value. The augmented contact state  $\mathbf{d}_t^i$  remains in the robot state  $\mathbf{x}_t$  throughout the single contact phase. When contact is terminated, the contact state is marginalized out of the robot state by:

$$\bar{\mathbf{x}}_{t_k}^{\text{new}} = M \bar{\mathbf{x}}_{t_k}, \quad \bar{P}_{t_k}^{\text{new}} = M \bar{P}_{t_k} M^\top, \quad M = \begin{bmatrix} I & 0 & 0 & 0 \\ 0 & I & 0 & 0 \\ 0 & 0 & I & 0 \end{bmatrix} \quad (10)$$

2) *Correction Model*: Once the endcap enters the contact phase, the state can be corrected using the right-invariant correction model:

$$\begin{aligned} Y_{t_k} &= X_{t_k}^{-1} b + V_{t_k} \\ \begin{bmatrix} h_p(L_t, \tilde{a}_t) \\ 0 \\ 1 \\ -1 \end{bmatrix} &= \begin{bmatrix} R_{t_k}^\top & -R_{t_k}^\top v_{t_k} & -R_{t_k}^\top p_{t_k} & -R_{t_k}^\top d_{t_k} \\ 0 & 1 & 0 & 0 \\ 0 & 0 & 1 & 0 \\ 0 & 0 & 0 & 1 \end{bmatrix} \begin{bmatrix} 0 \\ 0 \\ 1 \\ -1 \end{bmatrix} \\ &+ \begin{bmatrix} J_p(L_t, \tilde{a}_t) w_{t_k}^a \\ 0 \\ 0 \end{bmatrix}, \end{aligned} \quad (11)$$

The linearized measurement matrix  $H$  and the noise matrix  $N_k$  are:

$$\begin{aligned} H &= [0 \quad 0 \quad -I \quad I], \\ \bar{N}_k &= \bar{R}_{t_k} J_p(L_t, \tilde{a}_t) \text{Cov}(w_{t_k}^a) J_p(L_t, \tilde{a}_t)^\top \bar{R}_{t_k}^\top. \end{aligned} \quad (12)$$

Finally, the RI-EKF contact correction can be calculated using the following:

$$\begin{aligned} \bar{X}_{t_k}^+ &= \exp(L_{t_k} (\bar{X}_{t_k} Y_{t_k} - b)) \bar{X}_{t_k}, \\ P_{t_k}^{r+} &= (I - L_{t_k} H) P_{t_k}^r (I - L_{t_k} H)^\top + L_{t_k} \bar{N}_k L_{t_k}^\top, \end{aligned} \quad (13)$$

where the Kalman gain  $L_{t_k}$  and innovation covariance  $S_{t_k}$ ,

$$L_{t_k} = P_{t_k}^r H^\top S^{-1}, \quad S = H P_{t_k}^r H^\top + \bar{N}_k. \quad (14)$$

## V. SHAPE RECONSTRUCTION

### A. Optimization Formulation

To solve for  $h(L_t, \tilde{a}_t)$  as required in Eqn. (5) in Sec. IV-B, we developed a constrained optimization algorithm that utilizes cable length measurements and IMU acceleration data to estimate the position of endcaps in the body frame.

The intuition behind this optimization is that the distances between the estimated endcap positions should closely match the measured cable length. Additionally, the endcap positions and rods must satisfy a set of constraints to ensure the robot's shape, i.e., the endcap positions in the body

frame, are valid. The goal of the optimization problem in Eqn. (15) is to find the optimal set of endcap positions  $Q_t^* = \{\mathbf{q}_t^i \in \mathbb{R}^3 | i \in \{0, 1, 2, 3, 4, 5\}\}$ .

$$\text{minimize } \sum_{(i,j) \in \mathbb{E}} \left( \|\mathbf{q}_t^i - \mathbf{q}_t^j\| - \tilde{l}_t^{ij} \right)^2 \quad (15a)$$

$$\text{s.t. } \mathbf{q}_t^0 = [0, 0, L_{\text{rod}}/2 - d_{\text{offset}}]^\top \quad (15b)$$

$$\mathbf{q}_t^1 = [0, 0, -L_{\text{rod}}/2 - d_{\text{offset}}]^\top \quad (15c)$$

$$\mathbf{q}_t^{2,3} > 0, \mathbf{q}_t^{3,3} < 0 \quad (15d)$$

$$\mathbf{q}_t^{4,3} > 0, \mathbf{q}_t^{5,3} < 0 \quad (15e)$$

$$\|\mathbf{q}_t^0 - \mathbf{q}_t^1\| = \|\mathbf{q}_t^2 - \mathbf{q}_t^3\| = \|\mathbf{q}_t^4 - \mathbf{q}_t^5\| = L_{\text{rod}} \quad (15f)$$

$$\langle (\mathbf{c}_t^{23} - \mathbf{c}_t^{01}) \times (\mathbf{c}_t^{45} - \mathbf{c}_t^{23}), \mathbf{q}_t^2 - \mathbf{q}_t^3 \rangle > 0 \quad (15g)$$

$$\langle (\mathbf{c}_t^{45} - \mathbf{c}_t^{23}) \times (\mathbf{c}_t^{01} - \mathbf{c}_t^{45}), \mathbf{q}_t^4 - \mathbf{q}_t^5 \rangle > 0 \quad (15h)$$

$$\langle (\mathbf{c}_t^{01} - \mathbf{c}_t^{45}) \times (\mathbf{c}_t^{23} - \mathbf{c}_t^{01}), \mathbf{q}_t^1 - \mathbf{q}_t^0 \rangle > 0 \quad (15i)$$

$$\langle \mathbf{q}_t^2 - \mathbf{q}_t^4, \mathbf{q}_t^5 - \mathbf{q}_t^1 \rangle > 0 \quad (15j)$$

$$\langle \mathbf{q}_t^0 - \mathbf{q}_t^2, \mathbf{q}_t^3 - \mathbf{q}_t^5 \rangle > 0 \quad (15k)$$

$$\langle \mathbf{q}_t^4 - \mathbf{q}_t^0, \mathbf{q}_t^1 - \mathbf{q}_t^3 \rangle > 0 \quad (15l)$$

### B. Optimization variable & objectives

$\mathbf{q}_t^i$  represents the body frame position of endcap  $s_i$  at time  $t$ . The set of positions to be optimized is  $Q_t = \{\mathbf{q}_t^i \in \mathbb{R}^3 | i \in \{0, 1, 2, 3, 4, 5\}\}$ . The flattened optimization variable  $\mathbf{q}_t := [\mathbf{q}_t^{0\top}, \mathbf{q}_t^{1\top}, \mathbf{q}_t^{2\top}, \mathbf{q}_t^{3\top}, \mathbf{q}_t^{4\top}, \mathbf{q}_t^{5\top}]^\top$ .

Consequently, the objective function minimizes the error between the measured endcap distances and the estimated endcap distances is denoted as  $\|\mathbf{q}_t^i - \mathbf{q}_t^j\|$ ,  $(i, j) \in \mathbb{E}$ , and the sensor reading of the nine actuation cables as  $\tilde{l}_t^{ij}$ .

### C. Constraints

The equality and inequality constraints of the optimization problem are the following:

**Endcap arrangement constraints:** Eqn. (15b)-(15c) represents the fixed coordinates of  $s_0, s_1$  in the body frame as demonstrated in Fig. 2. Eqn. (15d)-(15e) represents the third element(z-axis) of  $\mathbf{q}^2, \mathbf{q}^4$  and  $\mathbf{q}^3, \mathbf{q}^5$  are  $> 0$  and  $< 0$ , respectively, i.e.  $s_0, s_2, s_3$  are in the upper-half-plane,  $s_1, s_3, s_5$  are in the lower-half-plane of the body frame, as shown in Fig. 2.

**Rod length constraints:** Eqn. (15f) are constraints between endcaps. Rods in tensegrity robots are rigid elements. The distance between two rod-connected endcaps should be a constant length  $L_{\text{rod}}$  at any time.

**Geometric Constraints:** Eqn. (15g)-(15i) are geometric constraints to restrict the rods from crossing each other along the time. The  $\mathbf{c}_t^{ij}$  represents the coordinates of the center of the rigid bar  $r_{ij}$ . Therefore,  $\mathbf{c}_t^{23} - \mathbf{c}_t^{01}$  represents the vector from the center point of the rod  $r_{01}$ , to the center of rod  $r_{23}$ . Then, the chained center vector's cross-product should be pointing to the axial axis shown in Fig.5 instead of pointing to the opposite or radial direction. So, the dot product of the cross-product vector and the axial vector will remain positive.

**Chirality Constraints:** Eqn. (15j)-(15l) are chirality constraints. The tensegrity structures are twisted 3-prism, which

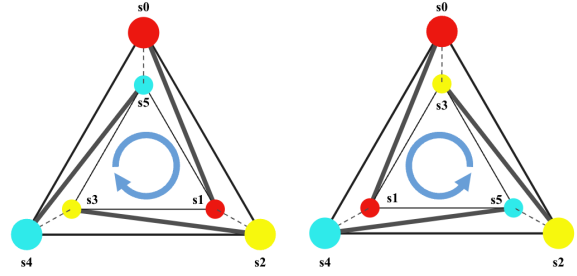


Fig. 4: Illustration of 3-bar tensegrity robot chirality from side-view. The right configuration is twisting counter-clockwise, the same structure we used in simulation and real-world robots.

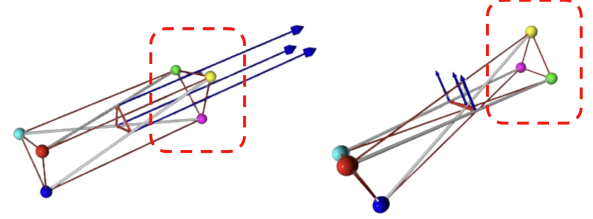


Fig. 5: Illustration of geometric constraints, red arrows represent the vectors chained to each rod center, blue arrows represent their cross-product vector. In the left figure, the geometric constraints are satisfied, with the cross-product vector pointing along the robot's axial direction. Conversely, the right figure demonstrates a switch to the opposite configuration. The endcap color in the circled area follows yellow-green-pink in the left figure, and yellow-pink-green in the right, which demonstrate the difference of the robot configuration.

have two twist directions as shown in Fig. 4. The tensegrity robot in simulation and the world is the same as the right configuration in Fig. 4, whose angles between two corresponding vectors(e.g.,  $\mathbf{q}^{24}, \mathbf{q}^{15}$ ) on the other side are acute which satisfy the constraints.

## VI. EXPERIMENTS

### A. Experiments Setup

We conducted a series of experiments with the cable-actuated tensegrity robot [6] in both simulation environments and real-world settings. The tensegrity robot consists of three bars, each measuring a length of 1.45m, 76mm in diameter, and weighing 4.0kg. An IMU (VectorNav VN-100) is attached to the drive unit at the center of the bar with red endcaps, providing linear acceleration and angular velocity data at 200Hz. The inelastic cables are actuated by brushless DC motors, and the encoders (AS5047P) report the cable lengths at 100Hz. Due to the current hardware limitations, onboard contact sensing has not yet been implemented. Instead, we rely on the Vicon motion capture system (MoCAP) for contact vector  $\mathbf{c}_t$ . The MoCaP system also records the ground-truth robot state  $\mathbf{x}_t$ , which is used to evaluate the performance of our state estimator. Future developments will incorporate contact sensors to enable fully onboard state estimation. In the Mujoco simulation, the physical properties of the robot including dimensions, mass, moment of inertia (MoI), and cable spring constants, as well as sensor biases and noises, are characterized to match the real-world tensegrity robot [6] (see Table. I for the parameters).

| Measurement Type        | Noise STD       |
|-------------------------|-----------------|
| Linear acceleration     | 0.043 $m/s^2$   |
| Angular velocity        | 0.002 $rad/s$   |
| Accelerometer bias      | 0.001 $m/s^3$   |
| Gyroscope bias          | 0.001 $rad/s^2$ |
| Contact linear velocity | 0.05 $m/s$      |

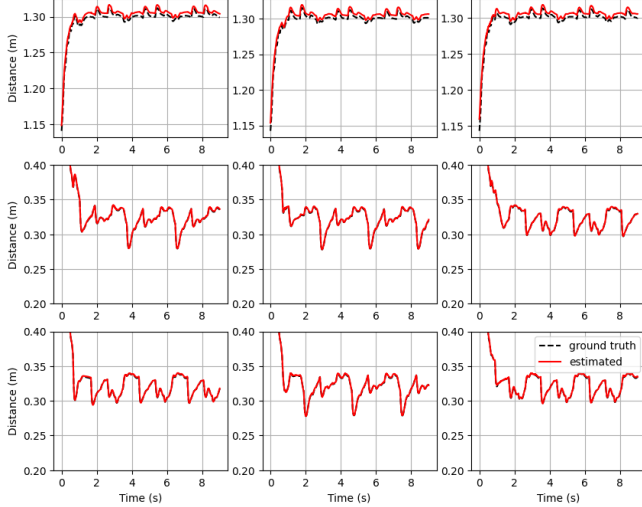


Fig. 6: Plots of the optimized cable lengths (red) compared to the ground truth distance between endcaps (black).

### B. Simulation Shape Reconstruction Results

We quantitatively evaluated shape reconstruction by comparing the distances between the estimated cable-connected endcap positions  $\|\mathbf{q}_t^i - \mathbf{q}_t^j\|$ ,  $(i, j) \in E$  to the ground-truth cable length  $l_t^{ij}$  from the simulation, as shown in Fig. 6. Without incorporating geometric constraints, significant shape reconstruction errors were observed due to the opposite chirality of the tensegrity structure, as illustrated in Fig. 5 (right). By incorporating the geometric constraints, the RMSE was reduced to 4.63 cm, which is negligible given the robot’s bar length of 1.45m.

### C. Simulation Pose Estimation Results

Our pose estimation method builds on the DRIFT [13] Invariant EKF framework. We conducted four simulation experiments: *move-forward*, *move-backward*, *right-turn*, and *left-turn*, each generating a different trajectory on flat ground. At the beginning of each sequence, the robot remained stationary for a few seconds for sensor initialization, such as accelerometer bias calibration. The robot was controlled via motor-actuated cables to perform predefined maneuvers. In the simulation, contacts were detected for the contact kinematic correction step in the Right Invariant EKF. Ground-truth pose, IMU measurements, cable length measurements, and contact vectors were published using ROS in the Mujoco simulation node. The shape reconstruction node subscribed to these inputs and published the robot shape  $\mathbf{Q}$ , while the Invariant EKF pose estimator estimated the robot pose in real-time, recording the estimated and ground-truth trajectories for later comparison. In this work, we employ evo [37] to

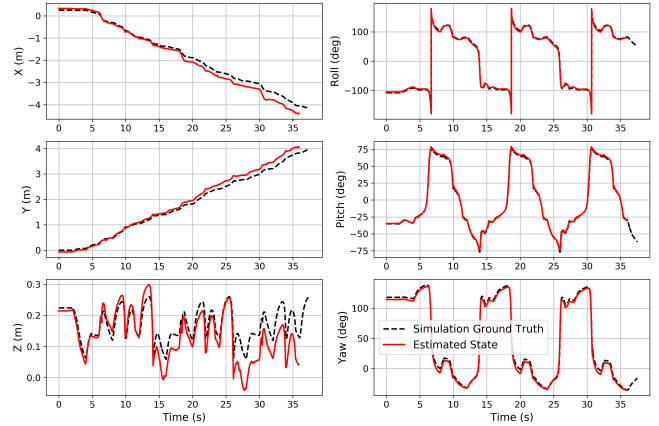


Fig. 7: Estimated position and orientation compared with ground truth in *forward* dataset.

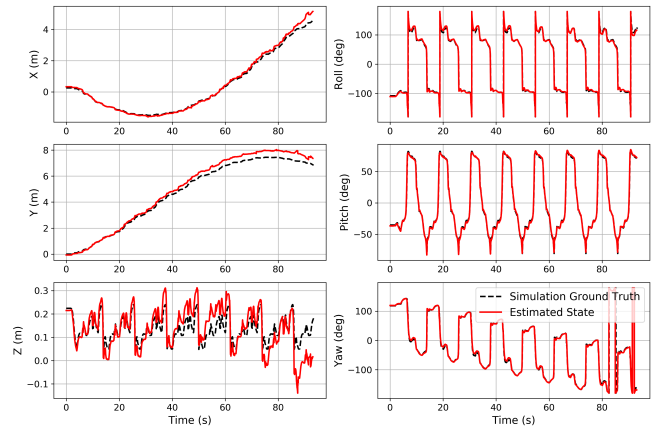


Fig. 8: Estimated position and orientation compared with ground truth in *right-turn* dataset.

align the initial segment of the estimated trajectory with the ground truth trajectory, as the initial pose is unobservable.

Fig. 7 presents the estimated position and orientation compared to the ground truth for the *forward* movement dataset, demonstrating robust tracking of both position and orientation. The deviations in the X and Y positions suggests the estimator is well-suited for translational movements, although larger discrepancies were observed along the Z-axis. The orientation estimation captures the oscillatory motions and are generally aligned with the ground truth.

For the *right-turn* dataset, as shown in Fig. 9, the robot demonstrated a longer 15.70-meter trajectory. Fig. 8 shows comparable performance to the *forward* dataset, despite a final drift of 0.76 meters over a 15.70-meter trajectory. The drift percentage remained low at 4.84% highlighting the estimator’s consistent accuracy even in more complex maneuvers.

### D. Real-world Pose Estimation Results

We conducted similar experiments in a real-world environment as in the *forward* simulation. Six Vicon motion capture cameras were set up, as shown in Fig. 11, with reflective markers installed on the tips of the robot’s endcaps. The MoCAP system tracked the markers to compute the ground-truth robot state and detect endcap-ground contacts,

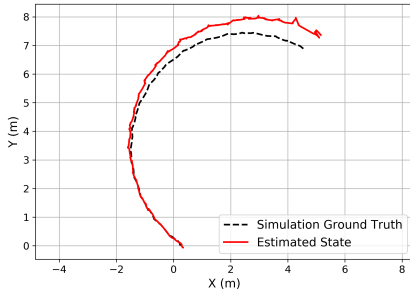


Fig. 9: Topview of *right-turn* dataset estimated trajectory compared with ground-truth.

TABLE II: Simulation and Real-world Experiments Statistics in Meter and Degree. We report the RMSE of Relative Pose Error(RPE) in the unit of drift per meter.

| Metric           | Forward | Backward | Left-turn | Right-turn | Forward-realworld |
|------------------|---------|----------|-----------|------------|-------------------|
| Traj. Length     | 7.50    | 6.74     | 18.61     | 15.70      | 5.02              |
| Final Drift      | 0.3275  | 0.3386   | 0.8221    | 0.7610     | 0.1174            |
| Drift Percentage | 4.37%   | 5.02%    | 4.42%     | 4.85%      | 2.34%             |
| RPE RMSE Trans.  | 0.0911  | 0.0936   | 0.1159    | 0.1022     | 0.1927            |
| RPE RMSE Rot.    | 2.86    | 3.72     | 3.94      | 3.18       | 10.84             |

as discussed in Sec. VI-A. The initialization procedures followed those described in Sec. VI-C. The VN-100 IMU and motor controller board within the tensegrity robot were connected to an Nvidia Jetson Nano Orin, with motion capture data synchronized via ROS. All collected data were stored for subsequent analysis.

As shown in Fig. 10, the state estimator performed reasonably well in estimating both position and orientation in real-world experiments. The  $x$  and  $y$  positions were accurately estimated, while the  $z$  position showed larger deviations (0.25m) over the 5-meter trajectory. In terms of orientation, the pitch angle shows discrepancies, especially in the latter part of the experiment. Despite these issues, the overall performance of the estimator remains promising when transitioning from simulation to real-world implementation. However, improvements in vertical position tracking remain necessary.

The root-mean-square-errors (RMSE) of the Relative Pose Error (RPE), reported in drift per meter, are summarized in Table. II. The average trajectory drift percentage (final drift/trajectory length) across all five datasets was 4.20%. Given the absence of prior work on dead-reckoning or odometry for tensegrity robots, we compared our results to state-of-the-art dead-reckoning and odometry algorithms for other robotic platforms, including a final drift of 3.18% in full-sized vehicles [13], 1.65% in legged robots [38], and 2.38% in the industrial robot Husky [13]. Despite the significantly increased structural and kinematic complexity of tensegrity robots, our state estimator’s performance remains comparable to these systems, demonstrating the robustness of our approach even in this challenging context.

We also performed runtime evaluations using a personal laptop with an i5-11400H CPU. Shape reconstruction required an average time of 4.1 ms, while InEKF propagation and contact correction took 11.33  $\mu$ s and 17.46  $\mu$ s, respectively. These results highlight the efficiency of the proposed algorithm, which operates at high frequencies and is suitable

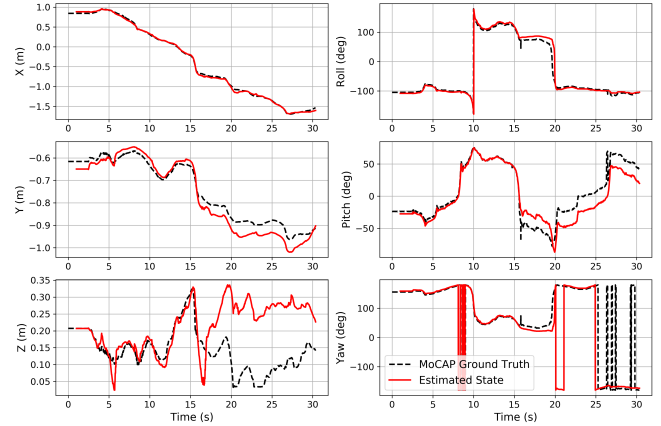


Fig. 10: Estimated position and orientation vs. MoCAP ground truth.

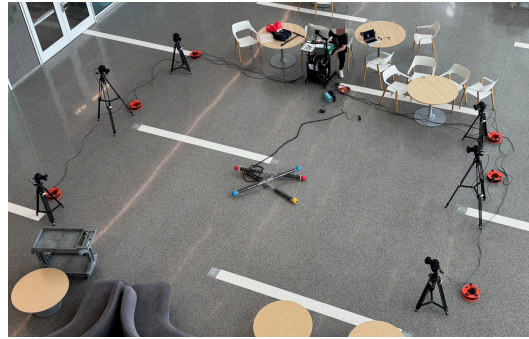


Fig. 11: Experiments setup with motion capture system to acquire ground truth position and orientation data for the tensegrity robots.

for onboard computing in untethered tensegrity robots. This is particularly important for enabling autonomous operations in resource-constrained environments.

## VII. CONCLUSION

We proposed a proprioceptive contact-aided Right Invariant EKF-based state estimator for tensegrity robots. Our approach utilizes an optimization method to reconstruct the shape of the 3-bar triangular prism tensegrity robot, providing kinematic information to the filter for correction. The estimator can estimate the robot’s pose in real-time in a real-world setting, using only IMU and motor encoder measurements along with contact information, and achieves an average positional drift percentage of 4.20%. This proprioceptive approach eliminates the need for off-board sensor setups, and delivers pose estimates comparable in accuracy to the state estimation of traditional rigid robots.

However, contact detection currently remains off-board due to hardware constraints. In future iterations, the development of onboard contact sensors will enable fully onboard state estimation for the tensegrity robot. Moreover, the current real-world experiments, while promising, are not yet comprehensive enough to fully demonstrate the state estimation capabilities across a wider range of maneuvers such as point turning or crawling, and different terrains like inclines and declines.

Future works will focus on incorporating contact endcap geometry into the reconstructed kinematics to improve estimation accuracy. Furthermore, we plan to explore onboard

contact detection methods, such as using contact sensors or data-driven approaches, to further enhance the robot's autonomous capabilities.

#### ACKNOWLEDGMENT

The authors would like to thank Hybrid Dynamic Robotics Lab team member Yilin Ma's help with the experiment environment setup.

#### REFERENCES

- [1] R. E. Skelton and M. C. De Oliveira, *Tensegrity systems*. Springer, 2009, vol. 1.
- [2] D. S. Shah, J. W. Booth, R. L. Baines, K. Wang, M. Vespignani, K. Bekris, and R. Kramer-Bottiglio, "Tensegrity robotics," *Soft robotics*, vol. 9, no. 4, pp. 639–656, 2022.
- [3] A. P. Sabelhaus, J. Bruce, K. Caluwaerts, Y. Chen, D. Lu, Y. Liu, A. K. Agogino, V. SunSpiral, and A. M. Agogino, "Hardware design and testing of superball, a modular tensegrity robot," in *World Conference on Structural Control and Monitoring (WCSCM)*, no. ARC-E-DAA-TN15339, 2014.
- [4] A. P. Sabelhaus, J. Bruce, K. Caluwaerts, P. Manovi, R. F. Firoozi, S. Dobi, A. M. Agogino, and V. SunSpiral, "System design and locomotion of superball, an untethered tensegrity robot," in *Proc. IEEE Int. Conf. Robot. and Automation*. IEEE, 2015, pp. 2867–2873.
- [5] M. Vespignani, J. M. Friesen, V. SunSpiral, and J. Bruce, "Design of superball v2, a compliant tensegrity robot for absorbing large impacts," in *Proc. IEEE/RSJ Int. Conf. Intell. Robots and Syst.* IEEE, 2018, pp. 2865–2871.
- [6] J. Mi, W. Tong, Y. Ma, and X. Huang, "Design of a variable stiffness quasi-direct drive cable-actuated tensegrity robot," *arXiv preprint arXiv:2409.05751*, 2024.
- [7] C. Paul, F. J. Valero-Cuevas, and H. Lipson, "Design and control of tensegrity robots for locomotion," *IEEE Trans. Robot.*, vol. 22, no. 5, pp. 944–957, 2006.
- [8] K. Kim, A. K. Agogino, D. Moon, L. Taneja, A. Toghyan, B. Dehghani, V. SunSpiral, and A. M. Agogino, "Rapid prototyping design and control of tensegrity soft robot for locomotion," in *IEEE international conference on robotics and biomimetics*. IEEE, 2014, pp. 7–14.
- [9] K. Kim, A. K. Agogino, A. Toghyan, D. Moon, L. Taneja, and A. M. Agogino, "Robust learning of tensegrity robot control for locomotion through form-finding," in *Proc. IEEE/RSJ Int. Conf. Intell. Robots and Syst.* IEEE, 2015, pp. 5824–5831.
- [10] C. Campos, R. Elvira, J. J. G. Rodríguez, J. M. Montiel, and J. D. Tardós, "ORB-SLAM3: An accurate open-source library for visual, visual-inertial, and multimap slam," *IEEE Trans. Robot.*, vol. 37, no. 6, pp. 1874–1890, 2021.
- [11] T. Shan, B. Englot, D. Meyers, W. Wang, C. Ratti, and D. Rus, "LIO-SAM: Tightly-coupled lidar inertial odometry via smoothing and mapping," in *Proc. IEEE/RSJ Int. Conf. Intell. Robots and Syst.* IEEE, 2020, pp. 5135–5142.
- [12] D. Li, X. Shi, Q. Long, S. Liu, W. Yang, F. Wang, Q. Wei, and F. Qiao, "DXSLAM: A robust and efficient visual slam system with deep features," in *Proc. IEEE/RSJ Int. Conf. Intell. Robots and Syst.* IEEE, 2020, pp. 4958–4965.
- [13] T.-Y. Lin, T. Li, W. Tong, and M. Ghaffari, "Proprioceptive invariant robot state estimation," *arXiv preprint arXiv:2311.04320*, 2023.
- [14] X. Xu, T. Zhang, S. Wang, X. Li, Y. Chen, Y. Li, B. Raj, M. Johnson-Roberson, and X. Huang, "Customizable perturbation synthesis for robust slam benchmarking," *arXiv preprint arXiv:2402.08125*, 2024.
- [15] L.-H. Chen, K. Kim, E. Tang, K. Li, R. House, E. L. Zhu, K. Fountain, A. M. Agogino, A. Agogino, V. SunSpiral *et al.*, "Soft spherical tensegrity robot design using rod-centered actuation and control," *Journal of Mechanisms and Robotics*, vol. 9, no. 2, p. 025001, 2017.
- [16] S. Hirai, Y. Koizumi, M. Shibata, M. Wang, and L. Bin, "Active shaping of a tensegrity robot via pre-pressure," in *IEEE/ASME International Conference on Advanced Intelligent Mechatronics*. IEEE, 2013, pp. 19–25.
- [17] J. Rieffel and J.-B. Mouret, "Adaptive and resilient soft tensegrity robots," *Soft robotics*, vol. 5, no. 3, pp. 318–329, 2018.
- [18] S. Lu, W. R. Johnson III, K. Wang, X. Huang, J. Booth, R. Kramer-Bottiglio, and K. Bekris, "6n-dof pose tracking for tensegrity robots," in *The International Symposium of Robotics Research*. Springer, 2022, pp. 136–152.
- [19] W. R. Johnson, A. Agrawala, X. Huang, J. Booth, and R. Kramer-Bottiglio, "Sensor tendons for soft robot shape estimation," in *2022 IEEE Sensors*. IEEE, 2022, pp. 1–4.
- [20] W.-Y. Li, A. Takata, H. Nabae, G. Endo, and K. Suzumori, "Shape recognition of a tensegrity with soft sensor threads and artificial muscles using a recurrent neural network," *IEEE Robotics and Automation Letters*, vol. 6, no. 4, pp. 6228–6234, 2021.
- [21] T. Qin, P. Li, and S. Shen, "Vins-mono: A robust and versatile monocular visual-inertial state estimator," *IEEE Trans. Robot.*, vol. 34, no. 4, pp. 1004–1020, 2018.
- [22] G. P. Roston and E. P. Krotkov, *Dead Reckoning Navigation For Walking Robots*. Department of Computer Science, Carnegie-Mellon University, 1991.
- [23] M. Camurri, M. Ramezani, S. Nobili, and M. Fallon, "Pronto: A multi-sensor state estimator for legged robots in real-world scenarios," *Frontiers in Robotics and AI*, vol. 7, p. 68, 2020.
- [24] M. Li and A. I. Mourikis, "High-precision, consistent ekf-based visual-inertial odometry," *Int. J. Robot. Res.*, vol. 32, no. 6, pp. 690–711, 2013.
- [25] M. Bloesch, M. Hutter, M. A. Hoepflinger, S. Leutenegger, C. Gehring, C. D. Remy, and R. Siegwart, "State estimation for legged robots: Consistent fusion of leg kinematics and imu," 2013.
- [26] R. Hartley, M. Ghaffari, R. M. Eustice, and J. W. Grizzle, "Contact-aided invariant extended kalman filtering for robot state estimation," *Int. J. Robot. Res.*, vol. 39, no. 4, pp. 402–430, 2020.
- [27] X. Yu, S. Teng, T. Chakhachiro, W. Tong, T. Li, T.-Y. Lin, S. Koehler, M. Ahumada, J. M. Walls, and M. Ghaffari, "Fully proprioceptive slip-velocity-aware state estimation for mobile robots via invariant Kalman filtering and disturbance observer," in *Proc. IEEE/RSJ Int. Conf. Intell. Robots and Syst.* IEEE, 2023, pp. 8096–8103.
- [28] L. Xiong, X. Xia, Y. Lu, W. Liu, L. Gao, S. Song, Y. Han, and Z. Yu, "IMU-based automated vehicle slip angle and attitude estimation aided by vehicle dynamics," *Sensors*, vol. 19, no. 8, p. 1930, 2019.
- [29] B. R. Tietz, R. W. Carnahan, R. J. Bachmann, R. D. Quinn, and V. SunSpiral, "Tetraspine: Robust terrain handling on a tensegrity robot using central pattern generators," in *IEEE/ASME International Conference on Advanced Intelligent Mechatronics*. IEEE, 2013, pp. 261–267.
- [30] X. Huang, W. R. Johnson, J. Booth, and R. Kramer-Bottiglio, "Live demonstration: Tensegrity state estimation," in *IEEE Sensors*. IEEE, 2022, pp. 1–1.
- [31] J. W. Booth, O. Cyr-Choiniere, J. C. Case, D. Shah, M. C. Yuen, and R. Kramer-Bottiglio, "Surface actuation and sensing of a tensegrity structure using robotic skins," *Soft Robotics*, vol. 8, no. 5, pp. 531–541, 2021.
- [32] A. Moldagalieva, D. Fadeyev, A. Kuzdeuov, V. Khan, B. Alimzhanov, and H. A. Varol, "Computer vision-based pose estimation of tensegrity robots using fiducial markers," in *IEEE/SICE International Symposium on System Integration (SII)*. IEEE, 2019, pp. 478–483.
- [33] K. Caluwaerts, J. Bruce, J. M. Friesen, and V. SunSpiral, "State estimation for tensegrity robots," in *Proc. IEEE Int. Conf. Robot. and Automation*. IEEE, 2016, pp. 1860–1865.
- [34] A. Barrau and S. Bonnabel, "An EKF-SLAM algorithm with consistency properties," *arXiv preprint arXiv:1510.06263*, 2015.
- [35] A. Barrau, "Non-linear state error based extended kalman filters with applications to navigation," Ph.D. dissertation, Mines Paristech, 2015.
- [36] Y. Luo, M. Wang, and C. Guo, "The geometry and kinematics of the matrix lie group  $se_k(3)$ ," *arXiv preprint arXiv:2012.00950*, 2020.
- [37] M. Grupp, "evo: Python package for the evaluation of odometry and slam." <https://github.com/MichaelGrupp/evo>, 2017.
- [38] S. Yang, Z. Zhang, Z. Fu, and Z. Manchester, "Cerberus: Low-drift visual-inertial-leg odometry for agile locomotion," in *Proc. IEEE Int. Conf. Robot. and Automation*. IEEE, 2023, pp. 4193–4199.